STEM image simulation by Bloch-wave method with layer-by-layer representation

Takao Morimura

Graduate School of Science and Technology, Nagasaki University, 1-14 Bunkyo-machi, Nagasaki 852-8521, Japan

TEL: +81-95-819-2636, FAX: +81-95-819-2634,

E-mail: **tmori@nagasaki-u.ac.jp**

Keywords: Bloch wave method, STEM, Bethe equation, EDX, inelastic electron scattering, layer-by-layer

Abstract

In a Bloch-wave-based STEM image simulation, a framework for calculating the cross section for any incoherent scattering process was formulated by Allen et al. They simulated the HAADF, BSE, EELS and EDX STEM images from the inelastic scattering coefficients. Furthermore, a skilful approach for deriving the excitation amplitude and block diagonalization in the eigenvalue equation were employed to reduce the computing time and memory. In the present work, we extend their scheme to a layer-by-layer representation for application to inhomogeneous crystals. Calculations for a multi-layer Si sample including a displaced layer was performed by multiplying Allen et al.'s block-diagonalized matrices. Electron intensities within the sample and EDX STEM images were calculated at various conditions. From the calculations, 3-dimensional STEM analysis was considered.

Introduction

The STEM image simulation by the dynamical electron diffraction was established by two individual methods: the multi-slice method [1-3] and the Bloch-wave method. The multi-slice method is effective for various objects including defects, but requires enormous computing time because parallel calculations in the STEM mode must be performed at each probe position. The Bloch-wave method reduces computing time and memory drastically for crystalline objects. However, images of defects demand large number of partial incident beams.

Pennycook et al. initially developed the simulation of high-angle annular dark-field (HAADF) STEM images by the Bloch-wave method [4,5]. Furthermore, Mitsuishi et al. [6] and Yamazaki et al. [7] extended HAADF STEM simulations based on the Bloch-wave method to layer-by-layer representation. In their method, the combination of the different types of layers can be calculated by multiplying matrices.

On the other hand, Allen et al. simulated electron energy-loss spectroscopy

(EELS), energy-dispersive X-ray spectroscopy (EDX) and back-scattered electron (BSE) STEM images as well as HAADF STEM images by calculating the cross section for inelastic scattering [8,9]. They formulated a framework for calculating the cross section for any incoherent scattering process from the inelastic scattering coefficient. Furthermore, their method employed a skilful approach for deriving the excitation amplitude and block diagonalization in the eigenvalue equation. The present author extended Allen's scheme to a layer-by-layer representation and applied it for Si-Sb-Si multi-layer samples [10]. In the present work, I extend this method to multi-layer samples including atomic displacement. From the calculations, 3-dimensional STEM analysis is considered, which was experimentally and theoretically reported as the depth sectioning ideas in Refs. [11-15].

Methods

A wave function in the STEM simulation is calculated by the Bethe equation

$$\mathbf{AC} = 2K\mathbf{C}(\lambda^k)_D,$$

where $\mathbf{C}$ and $(\lambda^k)_D$ are the matrices of eigenvectors $C_{\mathbf{g}}^k$ and of the eigenvalues, respectively. The subscript D indicates diagonal. K is the averaged wave number in the crystal. Findlay et al. [9] presented the reflections in STEM mode as

$$\mathbf{g} = \mathbf{G} + \mathbf{q}_l,$$

where the capitalized vector $\mathbf{G}$ denotes N physical reciprocal lattice vectors, and $\mathbf{q}_l$ denotes nearly continuous m vectors in the first Brillouin zone. The Bethe equation, whose dimension is $mN \times mN$, can be block diagonalized since the wave functions for different l do not interact with each other. Findlay et al. [9] presented the Bethe equation consisting of the m sub-matrices whose dimension are $N \times N$. We may now solve the m eigenvalue equation consisting of the sub-matrix such as

$$[\mathbf{A}(\mathbf{q}_l)][\mathbf{C}(\mathbf{q}_l)] = 2K[\mathbf{C}(\mathbf{q}_l)][\lambda^k(\mathbf{q}_l)]_D.$$

The total wave function is given by

$$\psi(\mathbf{K},\mathbf{R},\mathbf{r}_\perp,z)=\sum_{l=1}^{m}\sum_{k=1}^{N}\alpha^{l,k}(\mathbf{R})\exp[2\pi i\lambda^k(\mathbf{q}_l)z]\sum_{\mathbf{G}=1}^{N}C_{\mathbf{G}}^{k}(\mathbf{q}_l)\exp[2\pi i(\mathbf{G}+\mathbf{q}_l)\cdot\mathbf{r}_\perp], \quad (1)$$

where $\mathbf{r}_\perp$ and z indicate the positions along transverse and depth directions, respectively. $\mathbf{R}$ indicates the probe focus position. The excitation amplitude $\alpha^{l,k}$ was presented by Allen et al. [8].

Equation (1) is rewritten as a product of the $\mathbf{r}_\perp$-dependent term and the z-dependent amplitude $\varphi^{l,\mathbf{G}}(z)$ in Darwin's representation [16].

$$\psi(\mathbf{K},\mathbf{R},\mathbf{r}_\perp,z)=\sum_{l=1}^{m}\sum_{\mathbf{G}=1}^{N}\varphi^{l,\mathbf{G}}(z)\exp[2\pi i(\mathbf{G}+\mathbf{q}_l)\cdot\mathbf{r}_\perp], \quad (2)$$

where

$$\varphi^{l,\mathbf{G}}(z)=\sum_{k=1}^{N}\alpha^{l,k}(\mathbf{R})C_{\mathbf{G}}^{k}(\mathbf{q}_l)\exp[2\pi i\lambda^k(\mathbf{q}_l)z].$$

This can be expressed by block-diagonalized matrix form as in Ref. [10].

$$[\boldsymbol{\varphi}_n(z_n)]_{\mathbf{q}_l}=[\mathbf{C}_n(\mathbf{q}_l)]\{\exp[2\pi i\lambda_n^k(\mathbf{q}_l)z_n]\}_D[\boldsymbol{\alpha}_n(\mathbf{q}_l)]. \quad (3)$$

When a crystal is divided into many layers, from the boundary condition the excitation amplitudes of the n-th layer are expressed as follows:

$$\begin{aligned}
&[\boldsymbol{\alpha}_n(\mathbf{q}_l)]=[\mathbf{C}_n(\mathbf{q}_l)]^{-1}[\boldsymbol{\varphi}_n(0)]_{\mathbf{q}_l}\\
&=[\mathbf{C}_n(\mathbf{q}_l)]^{-1}[\boldsymbol{\varphi}_{n-1}(t_{n-1})]_{\mathbf{q}_l}\\
&=[\mathbf{C}_n(\mathbf{q}_l)]^{-1}[\mathbf{C}_{n-1}(\mathbf{q}_l)]\{\exp[2\pi i\lambda_{n-1}^k(\mathbf{q}_l)t_{n-1}]\}_D[\boldsymbol{\alpha}_{n-1}(\mathbf{q}_l)]\\
&=[\mathbf{C}_n(\mathbf{q}_l)]^{-1}[\mathbf{C}_{n-1}(\mathbf{q}_l)]\{\exp[2\pi i\lambda_{n-1}^k(\mathbf{q}_l)t_{n-1}]\}_D\cdots[\mathbf{C}_2(\mathbf{q}_l)]^{-1}[\mathbf{C}_1(\mathbf{q}_l)]\{\exp[2\pi i\lambda_1^k(\mathbf{q}_l)t_1]\}_D[\boldsymbol{\alpha}_1(\mathbf{q}_l)]
\end{aligned}$$

, (4)

where t_n is the thickness of the n-th layer. The excitation amplitude of the 1st-layer $\boldsymbol{\alpha}_1(\mathbf{q}_l)$ is obtained from the boundary condition between the upper surface of the sample and the vacuum [8]. The wave function in the n-th layer is calculated by substituting the z-dependent amplitude $\varphi_n^{l,\mathbf{G}}(z_n)$ into Eq. (2).

Equation (4) is very general formula. Any restrictions about the crystal structures

between the sequent layers are not required in Eq. (4). If the *n*-th layer in the sample of an elementary substance has an atomic displacement of $\boldsymbol{\tau}_n$ as shown in Fig. 1, the formulas are notably simplified. In this case, $[\mathbf{C}_n(\mathbf{q}_l)]$ in Eqs. (3) and (4) may be replaced by $[\exp[2\pi i(\mathbf{G}\cdot\boldsymbol{\tau}_n)]_D^{-1}[\mathbf{C}_1(\mathbf{q}_l)]$ in the same manner as Ref. [16] also in the STEM case. The diagonal matrix $[\exp(2\pi i\mathbf{G}\cdot\boldsymbol{\tau}_n)]_D$ indicates the phase change of structure factors due to the atomic displacement.

The cross section for inelastic scattering or EDX STEM signal intensity is calculated following the representation of Allen et al. [8-10]. In the present work, the off-diagonal elements of the Bethe matrix $[\mathbf{A}(\mathbf{q}_l)]$ were estimated using the atomic scattering factors by Doyle and Turner [17] and the absorption potentials by Humphreys and Hirsch [18]. The numbers of the physical reciprocal lattices (*N*) and of the nearly continuous vectors in the first Brillouin zone (*m*) were assumed to be 205 and 53, respectively, in zeroth-order Laue zone at [110] zone axis incidence. The accelerating voltage was assumed to be 200 kV. The atomic scattering factor for inelastic scattering included in the inelastic scattering cross section was approximately estimated as Fourier coefficients of Lorentzian or Gaussian profiles smeared by Debye-Waller factors [19]. The amplitude and the full-width at half maximum of the profiles for various elements were calculated by Oxley and Allen for EDX [20] and EELS [21]. We estimate the scattering factor for EDX from Ref. [20] and from the Debye temperatures Θ_{Si} = 645 K. The transfer function of the objective lens is defined in the same manner as in Rossouw et al. [22] and the underfocus is assumed to be negative.

Results

Figure 1 shows the sample used in the simulation, which is composed of a 3-layer Si stack along [110] in a diamond lattice. The 2nd layer has a hypothetical displacement of 0.05 nm along [001] direction. The thicknesses of the 1st, 2nd and 3rd layers were 4.5, 1 and 4.5

nm, respectively. The lattice constants were assumed to be 0.543 nm. Each layer was assumed to be free of strain.

Figure 2 shows the dependence of the electron intensities on the spherical aberration C_s calculated from Eq. (2). The horizontal and the vertical axes indicate the coordinate x along [001] and the depth z from the sample surface along [110], respectively. The brightness is proportional to the electron intensity at each point. The atomic columns in the 1st and 3rd layers are located at x = 0 and –0.136 nm. The centre of the STEM probe is located at x = 0 nm. The position of the displaced layers is shown at the right side of the figures. The simulation was performed for C_s = 0.1 mm (a), 0.01 mm (b) and 0.001 mm (c). The Scherzer focuses were assumed to be -19 nm (a), -6 nm (b) and –1.9 nm (c) $[1.2(\lambda C_S)^{1/2}]$, and the optimal cut-off apertures were assumed to be 7.6 nm^{-1} (a), 13.5 nm^{-1} (b) and 24 nm^{-1} (c) $[1.51(\lambda^3 C_S)^{-1/4}]$ such as in Ref. [10]. The STEM probe electrons at any C_s concentrated along z direction at x = 0 nm and even in the deep area of sample. The transverse resolution increases with decreasing C_s. The electron intensities seem to broaden along transverse direction around the displaced 2nd layer at C_s = 0.1 mm. The resolution along the z direction increased, and the focal depth of field decreased with decreasing C_s. At C_s = 0.001 mm, the depth of field attained was about 1 nm.

Figure 3 shows the defocus dependence of the electron intensities calculated at C_s = 0.001 mm when the centre of the STEM probe is located at x = 0 nm. The depths of the intensity maxima decreased with increasing defocus from -10 to 0 nm. If the potential at the atomic column and the spherical aberration are zero, the depths of intensity maxima are equal to the absolute defocus. Though, the depths were somewhat smaller than the absolute defocus for these effects, which were reported as a prefocus effect [23]. The high depth resolution or the narrow depth of field ~1 nm enabled us to calculate depth-sectioning STEM images at C_s = 0.001 mm.

Figure 4 shows the probe line-scan simulation of SiK EDX signals at C_s = 0.1 mm (a), 0.01 mm (b) and 0.001 mm (c). Horizontal and vertical axes indicate the probe position along [001] and the defocus, respectively. The intensive areas are observed around x = 0 and –0.136 nm. The transverse resolution increased with decreasing C_s. The displacements of the intensive areas corresponding to the atomic displacement are observed at C_s = 0.001 mm. They cannot be observed at C_s=0.1 and 0.01 mm because of the resolution limit with the depth of field. The displaced intensive area is nearly equal to the displaced layer thickness of 1 nm; however, the absolute defocus at the displaced area is larger than the depth of the displaced layer because of the prefocus effect as shown in Fig. 3. SiK intensities at x = 0 and –0.136 nm are attenuated around the displaced intensive area in (c).

Figure 5 shows the defocus dependence of the EDX STEM image simulations for the [110] zone axis calculated at C_s = 0.001 mm. Intensity maximum and minimum are indicated under each image. The bright spots are observed at atomic column positions in the 1st and 3rd layers at any defocus with high transverse resolution. The displaced spots are observed at Δf = -7 and -6 nm as indicated in Fig. 4 (c). These absolute defocuses are larger than the depth of the displaced layer because of the prefocus effect. Comparison of the defocus-dependent simulations of the STEM images with the experimental ones enabled us to obtain quantitative 3-dimensional information.

Figure 6 shows the probe line-scan simulation of SiK EDX signals at C_s = 0.001 mm for displaced layer thickness of 2 nm (a), 1 nm (b) and 0.2 nm (c). The displaced layers are located at the centre along the z-direction in the samples. The displaced intensive area along the vertical axis decreased with decreasing displaced layer thickness from (a) to (b). The intensities at x = 0 and –0.136 nm were concomitantly attenuated around Δf = -7 nm in them. The displaced intensive area in (c) is difficult to be observed. This is because of the resolution limit with the depth of field at C_S = 0.001 mm. The attenuate areas are slightly observed in (c).

Conclusions

Allen et al. skilfully formulated a framework for calculating the HAADF, BSE, EELS and EDX STEM images from the inelastic scattering coefficient by the Bloch wave method. We extended their scheme to a layer-by-layer representation. Calculations were performed for a multi-layer Si sample including a displaced layer by multiplying Allen et al.'s block-diagonalized matrices. Electron intensities within the sample and EDX STEM images were calculated at various conditions. Calculations of the STEM images revealed that 3-dimensional information can be obtained.

References

1 Kirkland E J, Loane R F and Silcox J (1987) Simulation of annular dark field STEM images using a modified multislice method. *Ultramicroscopy* 23: 77-96.

2 Anderson S C, Birkeland C R, Antist G R and Cockayne D J H (1997) An approach to quantitative compositional profiling at near-atomic resolution using high-angle annular dark field imaging. *Ultramicroscopy* 69: 83-103.

3 Ishizuka K (2002) A practical approach for STEM image simulation based on the FFT multislice method. *Ultramicroscopy* 90: 71-83.

4 Pennycook S J and Jesson D E (1991) High-resolution Z-contrast imaging of crystals. *Ultramicroscopy* 37: 14-38.

5 Nellist P D and Pennycook S J (1999) Incoherent imaging using dynamically scattered coherent electrons. *Ultramicroscopy* 78: 111-124.

6 Mitsuishi K, Takeguchi M, Toda Y and Furuya K (2003) Layer-doubling method in ADF-STEM image simulation. *Ultramicroscopy* 96: 323-333.

7 Yamazaki T, Watanabe K, Kuramochi K and Hashimoto I (2006) Exteded dynamical HAADF STEM image simulation using the Bloch-wave method. *Acta Cryst*. A 62: 233-236.

8 Allen L J, Findlay S D, Oxley M P and Rossouw C J (2003) Lattice-resolution contrast from a focused coherent electron probe. Part I. *Ultramicroscopy* 96: 47-63.

9 Findlay S D, Allen L J, Oxley M P and Rossouw C J (2003) Lattice-resolution contrast from a focused coherent electron probe. Part II. *Ultramicroscopy* 96: 65-81.

10 Morimura T and Hasaka M (2009) Bloch-wave-based STEM image simulation with layer-by-layer representation. *Ultramicroscopy* 109: 1203-1209.

11 van Benthem K, Lupini A R, Kim M, Baik H S, Doh S, Lee J H, Oxley M P, Findlay S D, Allen L J, Luck J T and Pennycook S J (2005) Three-dimensional imaging of individual hafnium atoms inside a semiconductor device. *Appl. Phys. Lett.* 87: 034104-1-3.

12 Borisevich A Y, Lupini A R and Pennycook S J (2006) Depth sectioning with the aberration-corrected scanning transmission electron microscope. *Proc. Nat. Acad. Sci.* 103:

3044-3048.

13 Borisevich A Y, Lupini A R, Travaglini S and Pennycook S J (2006) Depth sectioning of aligned crystals with the aberration-corrected scanning transmission electron microscope. *J. Electron Microscopy* 55: 7-12.

14 D'Alfonso A J, Findlay S D, Oxley M P, Pennycook S J, van Benthem K and Allen L J (2007) Depth sectioning in scanning transmission electron microscopy based on core-loss spectroscopy. *Ultramicroscopy* 108: 17-28.

15 Xin H L and Muller D A (2009) Aberration-corrected ADF-STEM depth sectioning and prospects for reliable 3D imaging in S/TEM. *J. Electron Microscopy* 58: 157-165.

16 Hirsch P B, Howie A, Nicholson R B, Pashley D W and Whelan M J (1977) *Electron Microscopy of Thin Crystals*. (Krieger Publishing Company, Malabar, Florida.)

17 Doyle P A and Turner P S (1968) Relativistic Hatree-Fock X-ray and Electron Scattering Factors. *Acta Cryst*. A 24: 390-397.

18 Humphreys C J and Hirsch P B (1968) Absorption Parameters in Electron Diffraction Theory. *Philos*. *Mag*. 18: 115-122.

19 Rossouw C J, Forwood C T, Gibson M A and Miller P R (1997) Generation and absorption of characteristic X-rays under dynamical electron diffraction conditions. *Micron* 28: 125-137.

20 Oxley M P and Allen L J (2000) Atomic scattering factors for *K*-shell and *L*-shell ionization by fast electrons. *Acta Cryst*. A 56: 470-490.

21 Oxley M P and Allen L J (2001) Atomic scattering factors for *K*-shell and *L*-shell electron energy-loss spectroscopy. *Acta Cryst*. A 57: 713-728.

22 Rossouw C J, Allen L J, Findlay S D and Oxley M P (2003) Channelling effects in atomic resolution STEM. *Ultramicroscopy* 96: 299-312.

23 Cosgriff E C and Nellist P D (2007) A Bloch wave analysis of optical sectioning in aberration-corrected STEM. *Ultramicroscopy* 107: 626-634.

Figure legends

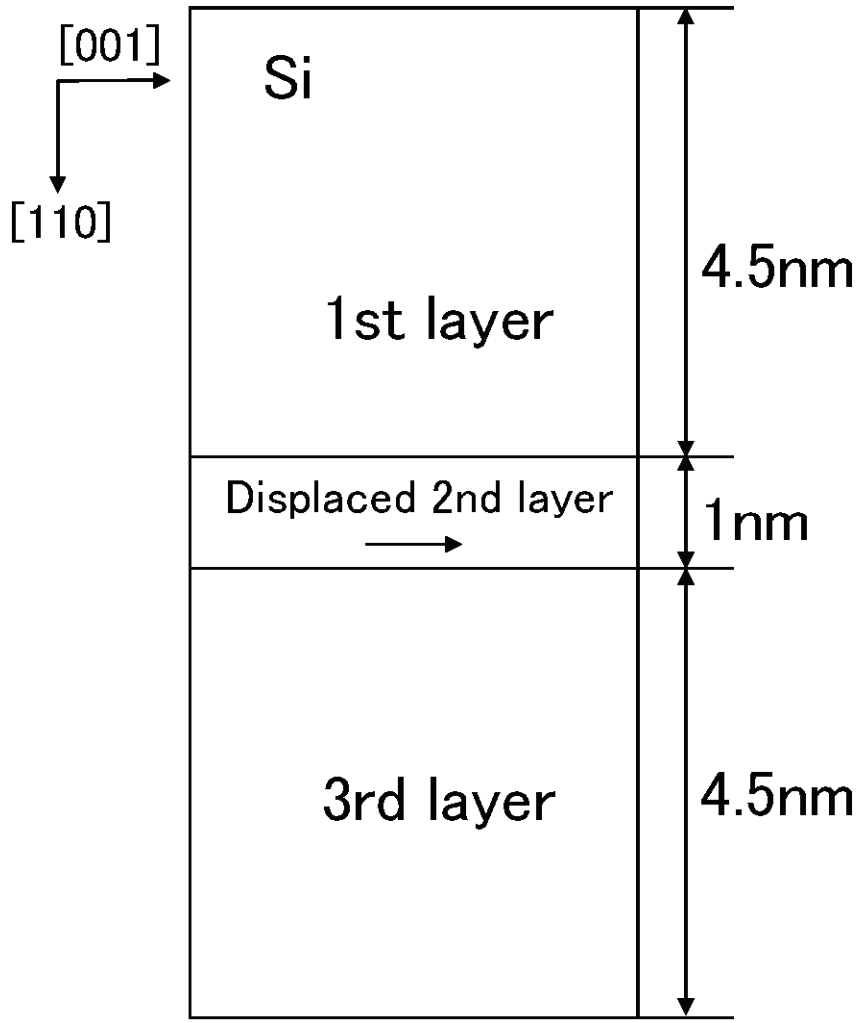

Fig. 1. Scheme of the simulated multi-layer Si sample. It is composed of 3-layer stack along [110] in a diamond lattice. The 2nd layer has a hypothetical displacement of 0.05 nm along [001]. The thicknesses of the 1st, 2nd and 3rd layers were 4.5, 1 and 4.5 nm, respectively.

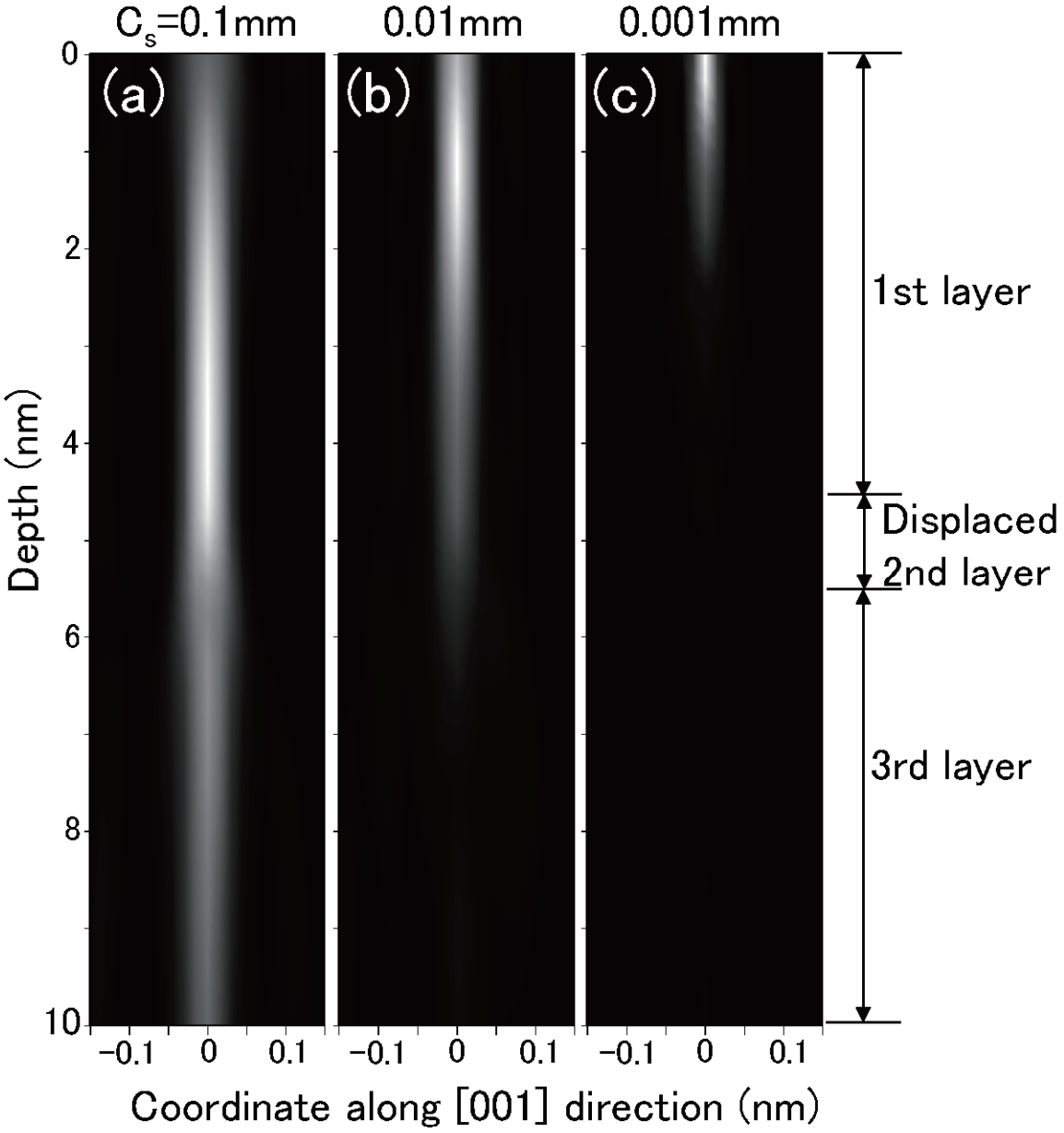

Fig. 2. Calculated electron intensities in the Si stack sample of Fig. 1. The calculations were performed in the spherical aberrations of 0.1 mm (a), 0.01 mm (b) and 0.001 mm (c) with Scherzer focuses and optimal cut-off apertures. The horizontal and the vertical axes indicate coordinates along [001] and the depth from the sample surface along [110], respectively. The atomic columns are located at x = 0 and –0.136 nm in the 1st and 3rd layers. The center of the STEM probe is located at x = 0 nm. The position of the 3 layers is shown at the right side of the figures.

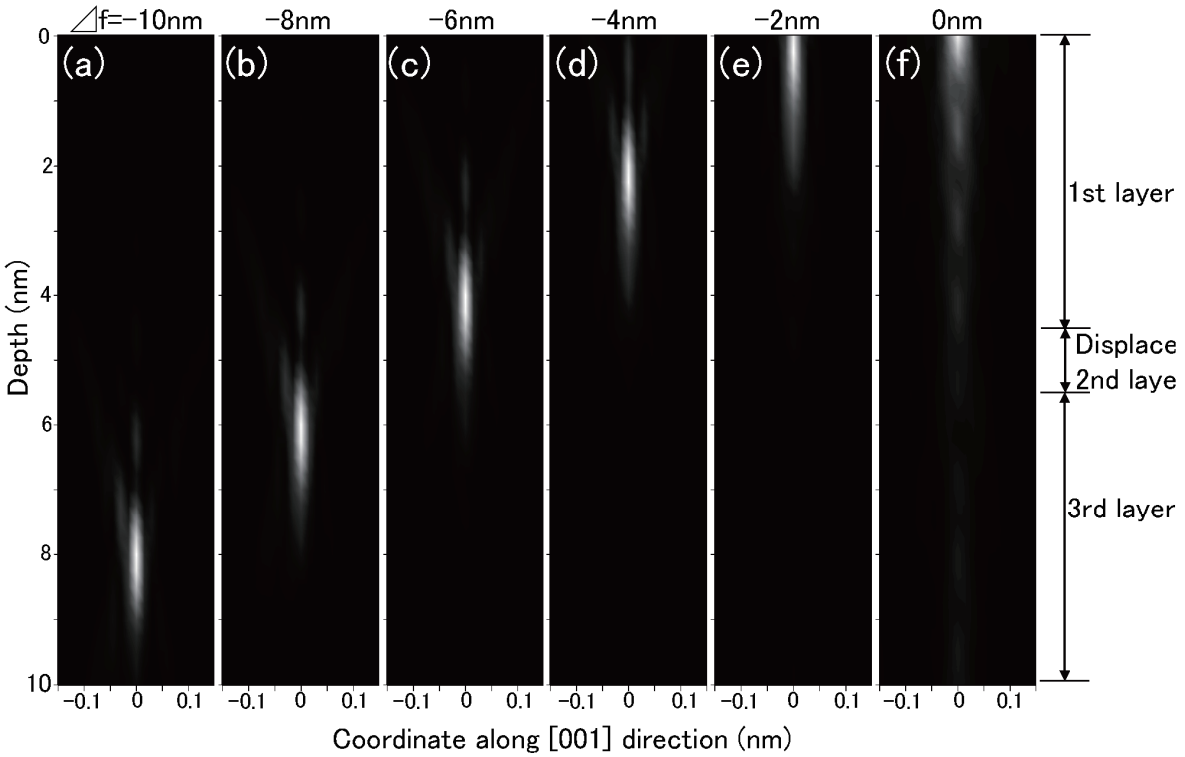

Fig. 3. Calculated electron intensities in the Si stack sample of Fig. 1. The calculations were performed at the defocuses of -10 nm (a), -8 nm (b), -6 nm (c), -4 nm (d), -2 nm (e) and 0 nm (f) with spherical aberration 0.001 mm and optimal cut-off aperture 24 nm^{-1}. The horizontal and the vertical axes indicate coordinates along [001] and the depth from the sample surface along [110], respectively. The atomic columns are located at x = 0 and –0.136 nm in the 1st and 3rd layers. The center of the STEM probe is located at x = 0 nm. The position of the 3 layers is shown at the right side of the figures.

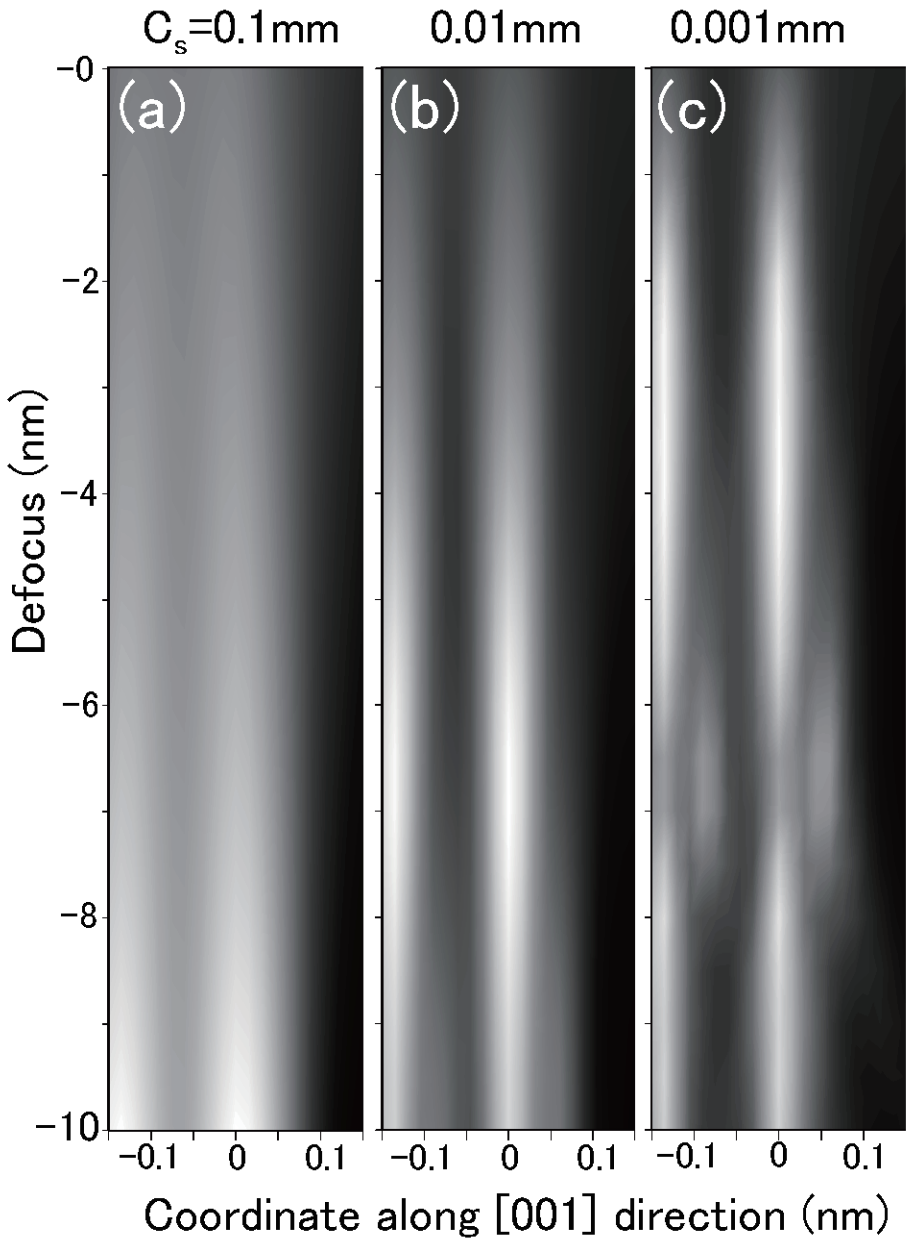

Fig. 4. Probe line-scan simulation of SiK EDX signal in the Si stack sample of Fig. 1. The horizontal and the vertical axes indicate the coordinate along [001] and the objective lens defocus, respectively. The calculations were performed for spherical aberrations 0.1 mm (a), 0.01 mm (b) and 0.001 mm (c) and for optimal cut-off apertures.

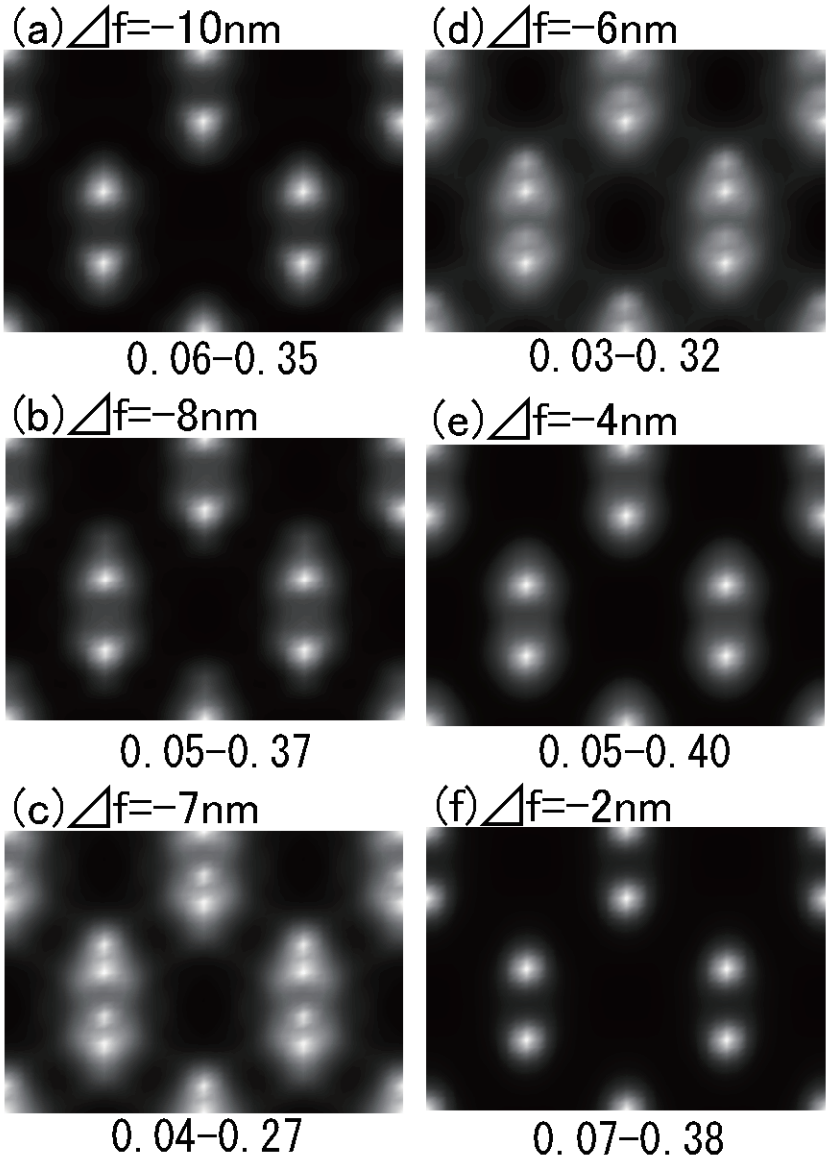

Fig. 5. Calculated EDX STEM image simulations for [110] zone axis incidence at the defocuses of -10 nm (a), -8 nm (b), -7 nm (c), -6 nm (d), -4 nm (e) and -2 nm (f) with spherical aberration 0.001 mm and optimal cut-off aperture 24 nm^{-1}. Intensity maximum and minimum are indicated under the each image.

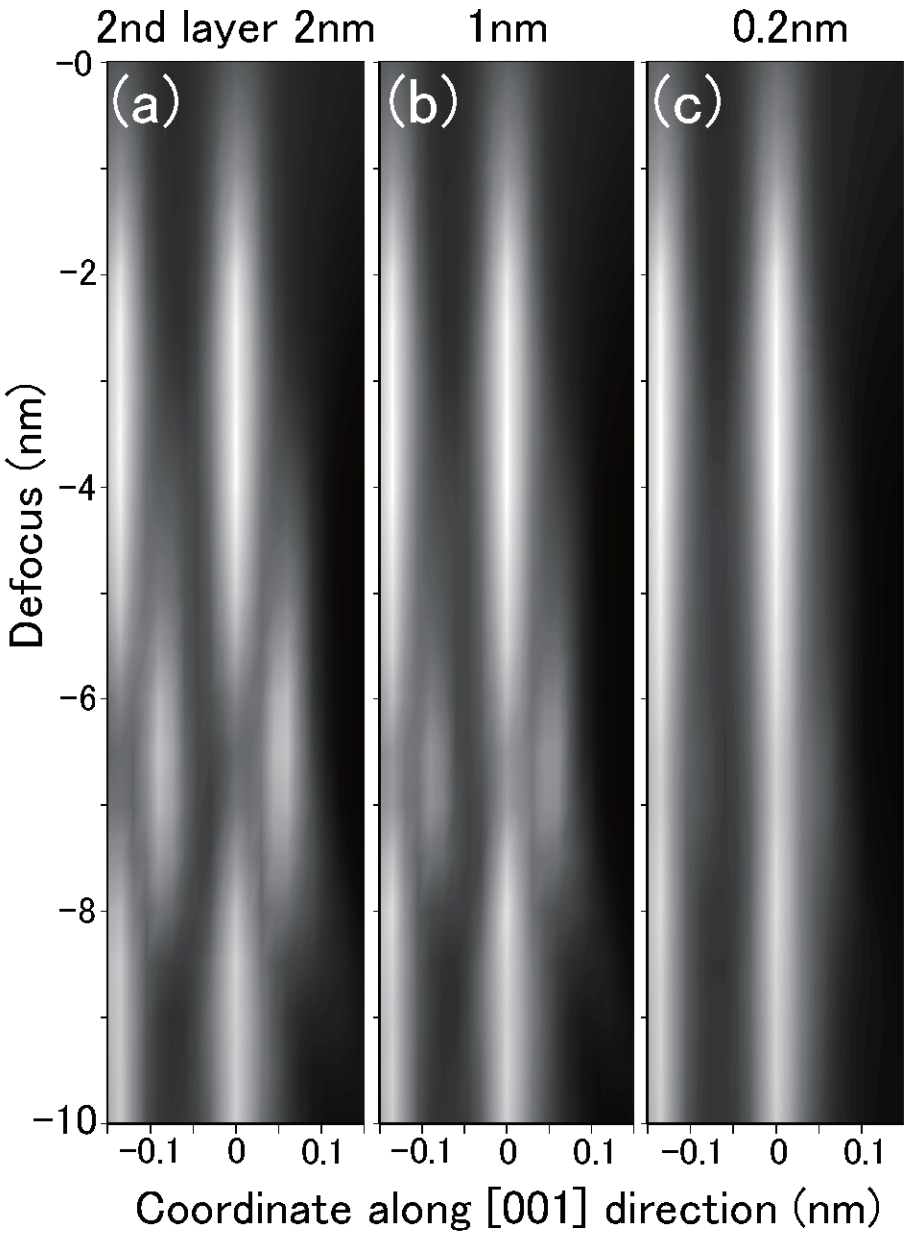

Fig. 6. Probe line-scan simulation of SiK EDX signals for displaced 2nd layer thickness of 2 nm (a), 1 nm (b) and 0.2 nm (c). The displaced 2nd layers are located on the center along the *z*-direction in the samples. The horizontal and the vertical axes indicate the coordinate along [001] and the objective lens defocus, respectively. The calculations were performed for spherical aberration 0.001 mm and optimal cut-off aperture 24 nm^{-1}.